Solid State Ionics 225 (2012) 136–140

Contents lists available at SciVerse ScienceDirect

Solid State Ionics

journal homepage: www.elsevier.com/locate/ssi

Impact of Cr-poisoning on the conductivity of different $LaNi_{0.6}Fe_{0.4}O_3$ cathode microstructures

M.K. Stodolny [a,*], B.A. Boukamp [b], D.H.A. Blank [b], F.P.F. van Berkel [a]

[a] Energy research Centre of the Netherlands (ECN), Hydrogen and Clean Fossil Fuels P.O. Box 1, 1755 ZG, Petten, The Netherlands
[b] Department of Science and Technology & MESA+ Institute for Nanotechnology, University of Twente, 7500 AE, Enschede, The Netherlands

ARTICLE INFO

Article history:
Received 31 August 2011
Received in revised form 2 April 2012
Accepted 9 April 2012
Available online 9 May 2012

Keywords:
SOFC cathode
Cr-poisoning
Microstructure
Cr vapor transport
LNF
Perovskite

ABSTRACT

The microstructure of porous $LaNi_{0.6}Fe_{0.4}O_3$ (LNF) layers has a significant influence on the degree of the Cr-poisoning impact. The increase in the in-plane resistance and Cr accumulation in poisoned LNF-layers has been correlated with microstructural features. The Cr-poisoning impact is more severe in the case of a microstructure characterized by finer particles, higher porosity and larger particle surface area.

1. Introduction

The perovskite $LaNi_{0.6}Fe_{0.4}O_3$ (LNF) is being considered as a possible cathode and interconnect coating material for intermediate temperature SOFC (IT-SOFC) systems where relatively cheap interconnect materials, such as chromia-forming ferritic stainless steels, are used. High electronic conductivity, thermal expansion coefficient matching that of zirconia [1] and claimed high Cr-resistance [2–4] are the properties of LNF that enable its use as cathode current collecting layers, interconnect protective coatings and/or electrochemically active cathode layers. Furthermore, using the LNF material as a cathode is recommended for metal-supported SOFCs [5], due to the claimed high Cr-tolerance and good electrochemical performance obtained for LNF sintered at low temperatures [6].

However, an actual Cr-tolerance of the LNF material is debatable and controversial in the view of recent findings. Previous studies [7,8] have demonstrated the occurrence of solid-state reactivity of LNF with chromia at 800 °C. It has been found that LNF is chemically unstable at 800 °C when it is in direct contact with Cr_2O_3 as Cr-cations enter the perovskite phase replacing Ni- and Fe-cations. Other studies [9,10] showed a significant impact of Cr on the electronic conductivity of an LNF porous cathode layer at 800 °C. Vapor transport of Cr-species, originating from a porous metallic foam, and subsequent reaction with LNF resulted in a decrease of the electronic conductivity of the LNF layer. Cr-attack at the LNF grain surface resulted in a replacement of Ni by Cr in the perovskite lattice. Formation of a Cr-substituted LNF phase, with a significantly lower electronic conductivity, has led to a serious deterioration of the in-plane conductivity of the porous LNF layer.

In the later study it has also been anticipated that the particle size distribution would have a considerable influence on the rate and magnitude of the electronic conductivity loss. Therefore, the role of the microstructure on the conductivity deterioration is a subject of the present work and will be discussed as a follow-up study of ref. [10]. To create a wide range of samples with different micro-structural parameters (porosity, internal surface area, etc.) two sets of the LNF powder with different morphology were sintered at different temperatures.

To analyze and compare different LNF microstructures a proper quantitative micro-structural analysis method has to be chosen. In the present study a 2D SEM approach has been used. The investigated samples were represented by a simple binary system: LNF particles (black) and pores (white). The 2D SEM micrographs provided sufficient quantitative microstructural information allowing the relative comparison of different LNF layers. The degree of Cr-poisoning and the in-plane resistance increase of the LNF layer has been directly correlated with the quantitative microstructural features.

2. Experimental

2.1. Sample preparation

LNF layers were prepared using $LaNi_{0.6}Fe_{0.4}O_3$ powder (Praxair, 99.9% purity). The mechanical support used during the conductivity

* Corresponding author. Tel.: +31 224 564074; fax: +31 224 568489.
E-mail address: stodi@wp.pl (M.K. Stodolny).

0167-2738/$ – see front matter © 2012 Elsevier B.V. All rights reserved.
doi:10.1016/j.ssi.2012.04.004

measurements was composed of a tape cast 3 mol% yttria stabilized zirconia (3YSZ) layer. The 3YSZ layer was sintered at 1500 °C for 1 h resulting in an electrolyte disc of 25 mm diameter and 90 μm thickness. The sintered 3YSZ layer was subsequently covered with a 2 μm thick $Gd_{0.4}Ce_{0.6}O_{1.8}$ (40GDC) barrier layer by means of screen printing followed by sintering at 1300 °C for 1 h. To obtain LNF layers with different microstructures the following variations were introduced: *(i)* the as received LNF powder was pretreated by a calcination step at 800 °C for 1 h in air, *(ii)* the particle size and the degree of LNF powder dispersion in the screen print paste (powder dispersed in an alcohol-binder solution) was varied by introducing a milling step using a Dispermat (VMA-Getzmann GmbH) milling system, *(iii)* the obtained LNF pastes (LNF-paste-I and LNF-paste-II) were screen printed on top of the 40GDC barrier layer and sintered in air either at 1150 or 1250 °C for 1 h. Based on these variations *(i)–(iii)* four microstructures were selected and referred to as: LNF-A (calcined, milled, 1250 °C), LNF-B (calcined, milled, 1150 °C), LNF-C (as received, unmilled, 1250 °C), LNF-D (as received, unmilled, 1150 °C). Resulting LNF perovskite layers formed a 10 mm wide strip with a thickness in a range of 15–25 μm. To allow measurements of the LNF layer resistance gold contacts were attached as described elsewhere [9,11].

2.2. Resistance measurements

The resistance measurements procedure has been presented in the previous publication [10]. For Cr-poisoning experiments (exposure in dry air at 800 °C for 300 h) an ITM-14 ferritic FeCr-based alloy in the form of a porous foam (Plansee AG, Reutte, Austria [12]) was used as a Cr source. For each of the Cr-poisoning experiments a freshly cut and pre-oxidized ITM-14 foam was used. Details of the ITM-14 samples treatment were described in ref. [10].

2.3. Microstructural and compositional characterization

To characterize the porosity of LNF-layers two different approaches were used. The macroscopic geometrical porosity was obtained from the density of the LNF layer which was calculated from geometrical dimensions, measured weight and the theoretical density of $LaNi_{0.6}Fe_{0.4}O_3$. On a microscopic level the microstructural porosity was determined by the 2D image analysis (ImageJ software [13]) of SEM micrographs (JEOL JSM 6330F FEG-SEM) of the LNF layers' surface.

The elemental composition of the LNF-layers exposed to Cr volatile species was obtained by scraping off the LNF-layer and analyzing the elemental composition of the resulting powder by means of inductively coupled plasma-optical emission spectroscopy (ICP-OES), using a Varian Vista AX PRO CCD.

3. Results and discussion

3.1. Microstructure characterization

Table 1 presents values of the geometrical porosity and the microstructural porosity for different LNF layers. LNF layers manufactured with a calcined and milled LNF powder (LNF-paste-I) were less porous compared to LNF layers prepared out of as received and unmilled LNF powder (LNF-paste-II) for each of the sintering temperature (1150 and 1250 °C). The calcination improved milling efficiency of the LNF powder which led to an increase in the sintering activity, manifested by obtaining lower porosities and thinner layers.

As shown in Fig. 1, higher sintering temperature of 1250 °C for both LNF-pastes (samples LNF-A and LNF-C) resulted in a more intensive grain growth. Thus broader necks and larger grains were formed. In case of layers sintered at the lower temperature of 1150 °C necks and grains were small and abundant (samples LNF-B and LNF-D). Furthermore, samples LNF-A and LNF-B prepared using LNF-paste-I possessed a homogenous and continuous microstructure. However, in case of samples LNF-C and LNF-D manufactured using LNF-paste-II, for which the as received powder was agglomerated, the sintering between LNF crystallites within the agglomerates occurred at lower temperatures than the sintering between the agglomerates. The sintering of the crystallites inside the agglomerates formed large and separate particles, which led to an inhomogenous microstructure with large cavities, as observed in Fig. 1 for samples LNF-C and LNF-D.

Table 1
Summary of the characteristics of different LNF-*i* microstructures (*i* = A–D).

Layer preparation				
Powder treatment	calcined		as received	
Paste	milled and mixed		unmilled, only mixed	
	LNF-paste-I		LNF-paste-II	
Sintering temperature (°C)	1250	1150	1250	1150
LNF-*i* layer type	LNF-A	LNF-B	LNF-C	LNF-D
Microstructural features				
Geometrical porosity (%)	31	39	45	53
Layer thickness *T* (μm)	16	21	18	22
Microstructural porosity (%)	22	25	29	34
Cr-content $^{(300\ h\ exposure\ at\ 800\ °C)}$ (at%)	0.8	3.8	3.1	4.3
$f_{\%bulk_{i\ Cr\ aff}}^{300\,h(125\ nm\ Cr\text{-}intrusion)}$ (%)	33	58	42	70

3.2. Correlation of Cr-content with microstructure of the LNF-layer

The Cr-content, after 300 h exposure to volatile Cr-species, was obtained for four different LNF-layers by means of an ICP-OES method (Table 1). In order to correlate the observed Cr-content with the different micro-structural features of the LNF-layers a simple approach was taken. In this approach the main important assumption is that the surface of the LNF-bulk of four different LNF-layers was identical in its chemical behavior towards Cr-incorporation. Therefore, the Cr-intrusion into the LNF-particles, after a certain exposure period, was assumed to be the same for all microstructures. An exposure time of 300 h results in a Cr-affected volume of the LNF-particles corresponding to an intrusion depth of circa 125 nm [10]. Consequently, the available Cr-exposed LNF surface area in the four different LNF-microstructures determines the overall extent of the Cr-affected volume of the LNF bulk. In order to determine the impact of the microstructure on the amount of incorporated Cr, it is important to obtain a quantitative description of the Cr-affected volume of the LNF-bulk. The quantification of the Cr-affected volume was obtained using SEM micrographs (Fig. 1), which were digitally processed with the ImageJ software. The steps in the image processing sequence (Fig. 2) and the quantification of the Cr-affected volume of the LNF-bulk were:

- Step 1) SEM micrographs were binarized by automatic thresholding (isodata algorithm [13]) assigning a black area to the LNF bulk and a white area to the pore. Then the microstructural porosity was determined as a (*pore area*)/(*total area*) ratio.
- Step 2) The threshold data were analyzed as follows: In the 2D-image pores were regarded as “particles” because they were occupying less than 50% of the analyzed frame area and were separated by the interconnected LNF bulk area. For each of the pores larger than 4 pixels an individual object number and an outline was automatically assigned. Each pore's outline represents the LNF-surface, which can react with volatile Cr-species during the Cr-exposure.
- Step 3) Each pore's outline, as obtained in step 2, was enlarged (orange area) by the given value of the Cr-intrusion depth, giving a representation in the 2D plot of the Cr-affected volume of the LNF-bulk.
- Step 4) The obtained orange area was overlaid on the black area of the bulk (determined in step 1) representing ipso facto the Cr-affected volume of the LNF-bulk. The fraction of the LNF-bulk affected by Cr

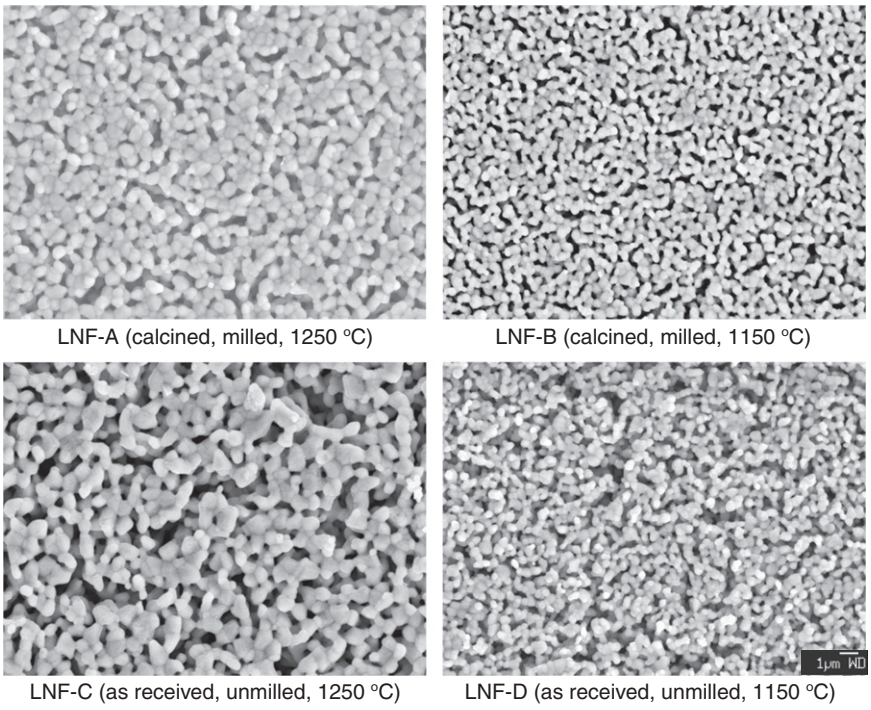

Fig. 1. SEM micrographs of the four different microstructures of LNF layers.

($f\%_{\text{bulk Cr-aff}}$), being the ratio between the Cr-affected LNF bulk ($A_{\text{bulk Cr-aff}}$) and the initial unaffected LNF bulk (A_{bulk}), should correlate with the amount of incorporated Cr according to the following relation:

$$f\%_{\text{bulk Cr-aff}} = \frac{A_{\text{bulk Cr-aff}}}{A_{\text{bulk}}} = \frac{\text{orange area}}{\text{black area}} \propto \text{Cr content}. \quad (1)$$

As observed in Fig. 3, the amount (in at%) of the incorporated Cr into the bulk of LNF after 300 h exposure (Table 1) correlates well with the calculated fraction of the Cr-affected LNF bulk area ($f\%_{\text{bulk, Cr-aff}}^{300\text{h}}$) (Table 1), validating the proposed approach and the relationship (1).

3.3. Correlation of in-plane resistance with microstructure of the LNF-layer

In order to correlate the layer resistance, in the Cr-free case (time 0 h) and in the Cr-intrusion case (time 300 h), with the layer microstructure the following considerations have to be taken into account:

Firstly, the resistance of a dense LNF-layer (R_{d}) is expressed as:

$$R_{\text{d}} = \varrho \frac{L}{A} = \varrho \frac{L}{T \cdot W}, \quad (2)$$

where ϱ denotes resistivity of the LNF-bulk, L is the length between contacts, and A represents the cross-sectional area of the dense bulk (A equals to the width W times the thickness T).

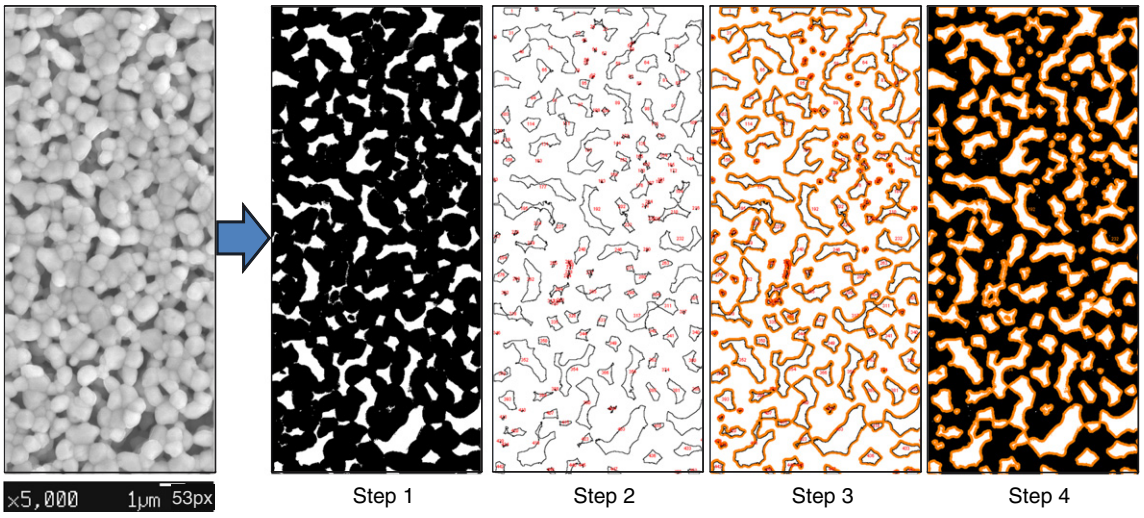

Fig. 2. Steps involved in the image processing of the SEM micrograph.

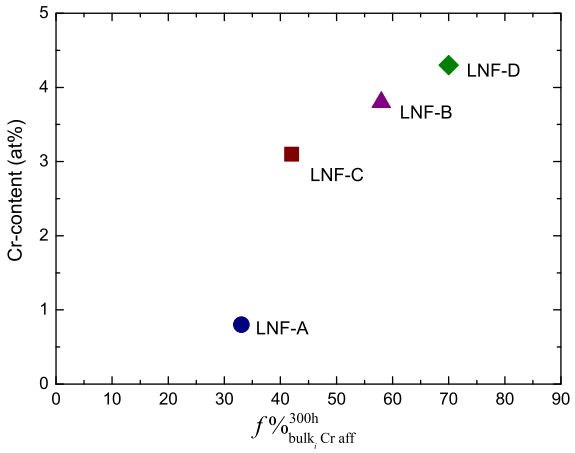

Fig. 3. Correlation of the amount of incorporated Cr into the bulk of LNF after 300 h with the calculated fraction of the Cr-affected area of the LNF bulk.

Secondly, the resistance of the porous LNF-layer with a fractional porosity ε, which has not been affected by Cr, is expressed as:

$$R_p^{0h} = \varrho\frac{L}{A_{bulk}^{0h}} = \varrho\frac{L}{(W\cdot T)\cdot(1-\varepsilon)}, \quad (3)$$

where A_{bulk}^{0h} is defined as the cross-sectional area corrected for the porosity. This is a first order approximation of the influence of the porosity on the in-plane electrical resistance, though some more complex formulations have been also reported in the literature [14,15].

For the four different LNF-*i* layers (i {*A*, *B*, *C*, *D*}) ϱ, *L*, *W* are constant, but *T* and ε varies due to differences in the microstructure. Therefore, by introducing the cross-sectional area specific resistance $ASR_{p,i}^{0h}$, which equals $R_{p,i}^{0h}\cdot W\cdot T_i$, Eq. (3) can be conveniently expressed as:

$$ASR_{p,i}^{0h} = \varrho L\cdot\frac{1}{1-\varepsilon_i}. \quad (4)$$

Thirdly, the resistance of a porous LNF-layer after 300 h of Cr-exposure can be expressed using modified Eq. (3) as:

$$R_{p,i}^{300h} = \varrho L\cdot\frac{1}{1-\varepsilon_i}. \quad (5)$$

The Cr-affected area ($A_{bulk\ Cr\text{-}aff}^{300h}$) is assumed here as non-conductive, because $\varrho_{LNF\text{-}Cr} \gg \varrho_{LNF}$ (0.02 Ωcm >>0.0017 Ωcm) [10], resulting effectively in a decrease of the cross-sectional area of the highly conductive LNF phase.

Assigning again $f\%_{bulk\ Cr\text{-}aff}^{300h} = A_{bulk\ Cr\text{-}aff}^{300h}/A_{bulk}^{0h}$ (similarly as in Eq. (1)), one can rewrite Eq. (5) as:

$$R_{p,i}^{300h} = \varrho\frac{L}{A_{bulk}^{0h}\cdot\left(1-f\%_{bulkCr-aff}^{300h}\right)}, \quad (6)$$

which can be further simplified, by replacing ϱ with Eq. (3), which results for the different LNF-*i* layers in the final expression:

$$R_{p,i}^{300h} = \frac{R_{p,i}^{0h}}{\left(1-f\%_{bulk_i\ Cr-aff}^{300h}\right)}. \quad (7)$$

Eq. (7) allows the estimation of the resistance at time 300 h based on the input data of the measured resistance at time 0 h and the fraction of the Cr-affected bulk at time 300 h as obtained from the image analysis in Table 1. This allows comparison between the measured and the calculated resistance at time 300 h.

3.3.1. Resistance as a function of microstructure at time 0 h (Cr-free case)

Fig. 4 presents the correlation of the resistance for different porous LNF-*i* layers obtained at time 0 h as a function of variable microstructure parameters according to Eq. (4). This correlation holds very well for both geometrical porosity values as well the microstructural porosity values (Table 1). Such a good agreement validates the use of the 2D image analysis approach.

3.3.2. Resistance evolution in Cr-containing atmosphere for different microstructures

Fig. 5 shows the resistance evolution in time for different porous LNF-*i* layers exposed at 800 °C in dry air to an ITM-14 Cr-source. All LNF-*i* layers exhibited a significant increase of the in-plane resistance within the first 50 h. Subsequently, a semi-linear resistance increase occurred in the time period of 100–300 h. The LNF-*i* layers were exposed only for 300 h as the previous study [10] reported a change in the evaporation behavior of the porous ITM-14 foam above 320 h.

The simulated values of the resistance at time 300 h ($R_{p,i}^{300h}$), calculated according to Eq. (7), showed a relatively good agreement with the measured resistance values at time 300 h (Fig. 5). The proposed approach (Section 3.3) helps to understand the observed differences in the resistance increase for different LNF-*i* layers. The extent of the resistance increase depended on the fraction of the Cr-affected LNF bulk area, which related with the microstructure. Therefore, the parameter $f\%_{bulk_i\,Cr\text{-}aff}^{300h}$ reflected a susceptibility of the given microstructure to the Cr incorporation.

However, in case of sample LNF-C the simulated resistance increase is underestimated. This might be due to the fact that in the current approach the tortuosity and the grains' connectivity was not taken into account. Compared to other samples, the microstructure of the LNF-C sample (Fig. 1) is inhomogeneous with large cavities, poor grain connectivity and fewer percolation pathways, which contributes probably much more to the total resistance increase.

4. Conclusions

The proposed 2D image analysis approach, to correlate the impact of Cr-poisoning on different LNF microstructures, turned out to be successful. Especially, the calculated fraction of the Cr-affected area correlates well with the measured Cr-content and also gives satisfactorily explanation for the observed differences in the resistance increase for different LNF-*i* layers. The fraction of the Cr-affected LNF bulk area characterizes well different microstructures from the view point of the Cr-poisoning susceptibility. This parameter $f\%_{bulk\ Cr\text{-}aff}$ reflects the microstructural porosity, particle size and the length of the outline of the LNF bulk, which corresponds with the exposed particle surface area. Therefore, this approach proved, explained and justified that the

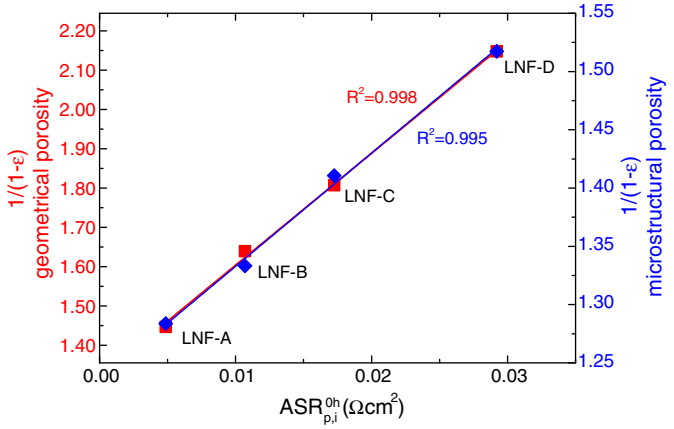

Fig. 4. Correlation of the resistance of different porous LNF-*i* layers obtained at time 0 h (Cr-free case) as a function of variable microstructure parameters.

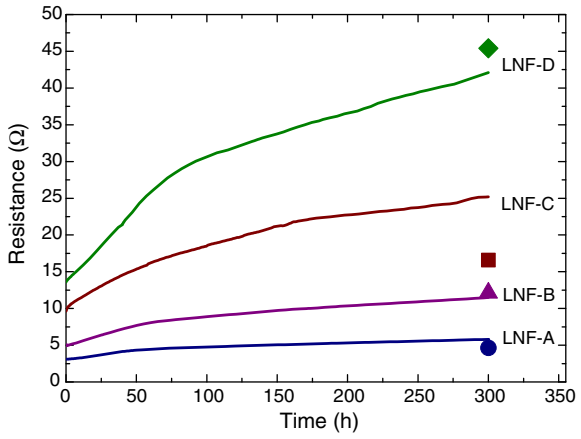

Fig. 5. Measured resistance evolution in time (solid line) of different LNF-*i* layers exposed to volatile Cr species in dry air at 800 °C. The colored symbols depict simulated values of resistance at time 300 h according to Eq. (7).

Cr-poisoning impact, in terms of the resistance increase and the Cr-accumulation, is more severe in case of microstructure characterized by finer particles, higher porosity and larger particle surface area.

The observed different Cr impact on different LNF microstructures could suggest that a microstructure with coarse particles and low surface area would be most Cr-tolerant. However, this study only considers the Cr impact on the in-plane resistance increase and the Cr-accumulation. In the electrochemically operated LNF cathode, the actual Cr-poisoning impact in terms of the overall cell performance degradation could be different, as shown in a recent paper [16].

Acknowledgements

This work was partly supported by the European Commission, as part of the European Project SOFC600 (SES6-CT-2006-020089), and partly supported by funding from ECN. Adrien Signolet is acknowledged for his involvement in this study during his traineeship at ECN. Wim Haije is thanked for helpful discussions. ECN Engineering & Services (Materials Testing & Consultancy group) is thanked for the SEM and ICP-OES analysis.

References

[1] R. Chiba, F. Yoshimura, Y. Sakurai, Solid State Ion. 124 (1999) 281.
[2] T. Komatsu, H. Arai, R. Chiba, K. Nozawa, M. Arakawa, K. Sato, Electrochem. Solid State Lett. 9 (2006) A9J.
[3] Y.D. Zhen, A.I.Y. Tok, S.P. Jiang, F.Y.C. Boey, J. Power. Sources 170 (2007) 61.
[4] G.Y. Laua, M.C. Tucker, C.P. Jacobson, S.J. Visco, S.H. Gleixner, L.C. DeJonghe, J. Power. Sources 195 (2010) 7540.
[5] M.C. Tucker, J. Power. Sources 195 (2010) 4570.
[6] H. Orui, K. Watanabe, R. Chiba, M. Arakawa, J. Electrochem. Soc. 151 (2004) A1412.
[7] M. Stodolny, F.P.F. van Berkel, B.A. Boukamp, ECS Trans. 25 (2) (2009) 2915.
[8] M.K. Stodolny, B.A. Boukamp, D.H.A. Blank, F.P.F. van Berkel, J. Electrochem. Soc. 158 (2) (2011) B112.
[9] M.K. Stodolny, F.P.F. van Berkel, B.A. Boukamp, ECS Trans. 35 (1) (2011) 2035.
[10] M.K. Stodolny, B.A. Boukamp, D.H.A. Blank, F.P.F. van Berkel, J. Power. Sources 196 (2011) 9290.
[11] F.P.F. van Berkel, M. Stodólny, M. Sillessen, J.P. Ouweltjes, Proceedings of the 8th European Solid Oxide Fuel Cell Forum, vol. A0621, European Fuel Cell Forum, 2008, p. 1.
[12] W. Glatz, G. Kunschert, M. Janousek, in: M. Mogensen (Ed.), Proc. 6th European Solid Oxide Fuel Cell Forum, European Fuel Cell Forum, Switzerland, 2004.
[13] M.D. Abramoff, P.J. Magelhaes, S.J. Ram, Biophotonics Int. 11 (2004) 36.
[14] J.M. Montes, F.G. Cuevas, J. Cintas, Appl. Phys. A 92 (2008) 375.
[15] D. Pérez-Coll, E. Sánchez-López, G.C. Mather, Solid State Ion. 181 (2010) 1033.
[16] M.K. Stodolny, B.A. Boukamp, D.H.A. Blank, F.P.F. van Berkel, J. Power. Sources 209 (2012) 120.